Rotor Integrity Design for a High-Speed Modular Air-Cored Axial-Flux Permanent-Magnet Generator

W. Fei, P. C. K. Luk, T. S. El-Hasan

Abstract— **The rotor integrity design for a high-speed modular air-cored axial-flux permanent-magnet (AFPM) generator is presented. The main focus is on establishing the radial and hoop stresses in the permanent magnets, retainment ring and back iron in the rotor, which become the key design issues at high operational speeds. To this end, approximate analytical formulae are employed for preliminary sizing of mechanical parameters, and two-dimensional (2-D) finite element analysis (FEA) models are used to optimize the values of the parameters. Then three-dimensional (3-D) FEA models are developed to verify the final design. Finally, based on the final design, a prototype AFPM is built for experimental validation, and mechanical integrity tests are undertaken. The results confirm the validity of the analytical and FEA models, as well as the overall design approach.**

Index Terms— **Air-cored, axial-flux permanent-magnet, high speed, hoop stress, radial stress, shrink fit.**

I. Introduction

ELECTRIC generating sets powered by small gas turbines are increasingly becoming prevalent reliable mobile electrical power sources , which can be employed in a wide rage of mission critical applications such as maintaining power electricity in emergency situations and disasters. High-speed air-cored axial flux permanent magnet (AFPM) machines, exploiting recent advances in high strength permanent magnets (PMs), have been considered one of the key solutions in meeting the demands of these power systems [1-7]. With an air-cored structure, the equivalent air-gap of the machine is enlarged, and both armature reaction and synchronous reactance will be significantly reduced accordingly, resulting in improved power factor. Consequently, the air-cored AFPM machine is favored to operate at a very high speed, with the option of directly driven by a gas turbine without reduction gears. This would lead to both high power density and reduced transmission losses, and hence higher efficiency. However, from electromagnetic design perspective, more PMs are needed to compensate the enlarged air-gap, which would increase the centrifugal force exerted in the rotor especially at very high rotational speed. As such, the mechanical design aspects of the rotor often become far more critical than the electromagnetic design aspects, in terms of reliability and safety of operations.

So far, most studies for air-cored AFPM machines focus on the electromagnetic aspects of analysis, optimization and design [4-6,8-16]. Some mechanical issues have been discussed in [3,7,17,18,19,20], they are considered only as supplementary to the electromagnetic design, which can only be justified for lower speed applications. On the other hand, mechanical design of rotor structures for high-speed surface-mounted radial-flux permanent-magnet (RFPM) machines have been studied in much detail [21,22]. Comprehensive rotor mechanical design has also been reported for a high-speed interior RFPM machine [23]. Moreover, AFPM machines normally possess relatively large and thin rotor disc and are particularly suitable for certain applications which benefit from a large aspect ratio structure. However, this also makes the rotor mechanical design of AFPM machine even more challenging than the RFPM counterpart. The rotor mechanical integrity design of the high-speed AFPM machines turns into the key design issue. Consequently, similar comprehensive work on rotor mechanical analysis and design for high-speed AFPM machines is highly demanded due to the fundamental geometric differences between the AFPM and RFPM configurations.

This paper concerns the mechanical design and analysis of the rotor of a modular three-phase 50kVA, 50000rpm AFPM generator, and thus complements an arguably more important design aspect lacking in previous studies focusing only on electromagnetic optimization. The main emphasis of this paper is on the mechanical parametric optimization of the magnet rotor disc, which includes the magnet retainment ring and the back iron disc. The optimization involves comprehensive stress analysis and shrink fit considerations of these rotor parts under high speed conditions. This is generally performed in a two-stage approach, first by means of approximate analytical formulae, then by simplified 2-D FEA models complemented with 3-D FEA models where appropriate for higher accuracy. Finally, the viability of the design approach is partially confirmed by experimental validation.

II. High-Speed Modular Air-Cored AFPM Generator

The construction of air-cored AFPM generators usually takes two forms: a magnet rotor disc rotating between two stator windings, or a stator winding disc sandwiched by two magnet rotor discs. The later form has been considered much more advantageous for high-speed applications since the back iron discs are rotating with the magnet rotor discs together. Thus, the eddy currents and hysteresis losses in the back iron discs can be pare down to a bare minimum. This also allows the use of solid back iron rather than laminated one for high speed operation.
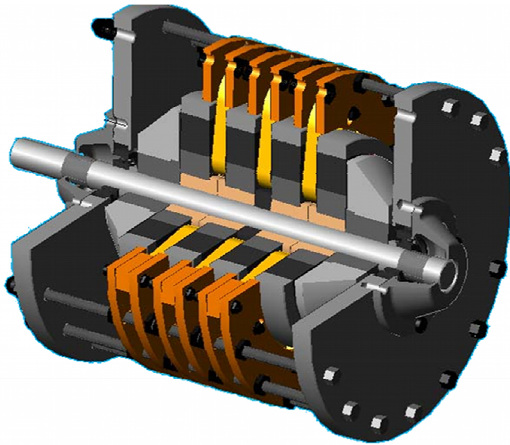
Fig. 1. Exploded view of the presented high-speed modular air-cored AFPM generator.

Fig. 2. Sectional view for the proposed magnet rotor disc

The three-phase air-cored AFPM generator under study is constructed in a modularized fashion by four magnet rotor discs and three winding stator discs, as shown in the exploded view in Fig.1. The modular configuration requires the robust and rigid magnet rotor discs should not be permanently fixed on the shaft, and therefore sliding fit is more feasible to allow for any further assembling or dismantling processes. A close sectional view of the magnet rotor disc of the proposed machine in Fig.1 is depicted in Fig. 2, which demonstrates a solid, rigid and high strength rotor hub is employed as connection between the magnet rotor disc and the shaft. The rotor hub is proposed, not only to be shrunk fit at the bore of the magnet rotor disc to prevent slippage of the magnet rotor at high operating speed, but also to be coupled with other rotor hubs on the same shaft through mechanical splines which are machined face to face. Additionally, the locking splines which are interference fit with the shaft .are designed to be coupled with rotor hubs. Hence the magnet rotor discs together with the rotor hubs will rotate rigidly with the shaft at the same speed.

The material EN24T is employed to contrast the shaft, and the mechanical property of the material is given in Table IV in the Appendix. Based on the shaft mechanical design guideline in [24] together with the results from the electromagnetic optimization previously performed, the shaft length has been designed as 150mm and the shaft diameter has been determined as 15mm. Hereafter, the spindle bearings, which are of the angular-contact, ceramic high-precession ball-bearing type, are considered as the most suitable. Consequently, the bearing type *HCS7002C.TP4S.UM* of 15 mm inner diameter is selected.

III. MAGNET ROTOR DISC DESIGN

A robust and rigid magnet rotor construction is paramount for high speed operations. High centrifugal forces will be exerted on the permanent magnets at high rotational speed. Consequently, wrapping sleeve or retainment ring must be employed to retain the magnets firmly at their positions. Generally, the material selected for the retainment ring of the rotor should have several distinctive mechanical properties:
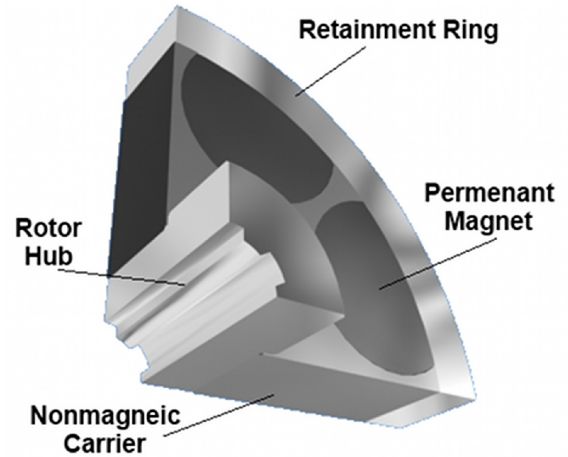
- high yield strength capability (>1800MPa), large modulus of elasticity, and acceptable percentage of elongation (>10%);
- materials with very low relative magnetic permeability and low magnetic saturation level;
- acceptable costs for raw materials and manufacture;
- low mass density.

Through extensive research, it is noted that among the non-magnetic materials, only composite materials such as carbon fiber can withstand high stresses. However, fabrication and assembly difficulties, and their associated impacts on performance, as well as the high costs, count severely against carbon fiber. It is found that a viable alternative offering higher manufacturability and lower cost with sufficient mechanical strength is provided by the low permeability magnetic material Maraging G125, the mechanical property of which is presented in Table V in Appendix. Once the type of the material has been decided for the ring, the minimum radial thickness of the ring and the amount of interference fit required to prevent separation between the magnet and ring at the design speed can be determined.

For the initial analytical stress calculations, the proposed magnet rotor disc geometry is simplified by assuming that the permanent magnet is continuously annular. For simplicity the rotor hub and magnet carrier are not considered in the analysis as they are non-essential parts that have negligible impacts on the overall design. Fig.3 shows the rotor structure for the analysis, where the inner disc represents the magnet where its dimensions are determined from the electromagnetic design [3,4], and the minimum outer radius R_{Ro} of the outer retainment ring needs to be determined to keep the hoop stresses in the ring below the specified design strength. An adequate safe margin of 5% for the operating speed is chosen in the calculations. The maximum hoop stress is to be found at the inner surface of the retainment ring, which is formulated as follows [25],

$$\sigma_{\theta T} = \frac{3+\nu}{4}\rho_R l_m \omega_m^2 \left[R_{Ro}^2 + \left(\frac{1-\nu}{3+\nu}\right)R_{mo}^2 \right] + \mathrm{Pr}_i \frac{R_{Ro}^2 + R_{mo}^2}{R_{Ro}^2 - R_{mo}^2} \qquad (1)$$

Fig. 3. Permanent magnet and retainment ring presented by concentric discs for stress analysis.

TABLE I
DESIGN DATA FOR A PARTICULAR MAGNET ROTOR DISC

R_{Ro}	R_{mo}	R_{mi}	P_{cont}	δ	l_m
55mm	47mm	27mm	138MPa	0.260mm	17mm

where ν and ρ_R are the Poisson's ratio and density of the retainment ring respectively, ω_m is the rotational speed of the rotor, R_{mo} is the magnet outer radius as well as retainment ring inner radius, and Pr_i is the pressure developed at the retainment ring inner radius from the permanent magnet, and can be derived as

$$Pr_i = \frac{\rho_m \omega_m^2 \left(R_{mo}^2 - R_{mi}^2 \right)\left(R_{mo} + R_{mi} \right)}{4 R_{mo}} \quad (2)$$

where ρ_m and R_{mi} are the density and inner radius of the magnet respectively. R_{Ro} for a given value of $\sigma_{\theta T}$ can be determined by solving equations (1) and (2) iteratively. Interference fit is employed to prevent the separation between the two discs while rotating at the rated speed, and the corresponding residual contact pressure P_{cont} should be sufficient to keep the magnets and all other parts below the retainment ring under negative pressure. By making $P_{cont}=Pr_i$, the total interference fit δ required to develop that pressure can be obtained as

$$\delta = \frac{2 R_{mo}^3 P_{cont} \left(R_{Ro}^2 - R_{mi}^2 \right)}{E \left(R_{Ro}^2 - R_{mo}^2 \right)\left(R_{mo}^2 - R_{mi}^2 \right)} \quad (3)$$

where E is the Young's modulus of the retainment ring. Then the temperature difference to allow for the retainment ring to slip over the magnet can be computed as

$$\Delta T = \frac{\delta}{R_{mo} \alpha_T} \quad (4)$$

where α_T is the thermal expansion coefficient of the material for the retainment ring. P_{cont} and δ can be evaluated by

Fig. 4. Axisymmetric FE stress analysis modeling of magnet and retainment ring.

equations (2) and (3) respectively. The data of a particular magnet rotor disc design for the proposed generator are given in Table I.

The analytical solutions of the total radial and hoop stresses distribution due to the residual and rotation at any point on the magnet and retainment ring can be derived based on Lams solutions for compound cylinders [25]. The total radial and hoop stresses in the retainment ring are expresses as

$$\sigma_{rT_{Ring}}(r) = \frac{P_{cont} R_{mo}^2}{(R_{Ro}^2 - R_{mo}^2)}\left(1 - \frac{R_{Ro}^2}{r^2}\right) + \frac{(3+\nu)}{8}\rho_m \omega_m^2 \left(R_{Ro}^2 + R_{mi}^2 - \frac{R_{Ro}^2 R_{mi}^2}{r^2} - r^2\right) \quad (5)$$

$$\sigma_{\theta T_{Ring}}(r) = \frac{P_{cont} R_{mo}^2}{(R_{Ro}^2 - R_{mo}^2)}\left(1 + \frac{R_{Ro}^2}{r^2}\right) + \frac{(3+\nu)}{8}\rho_m \omega_m^2 \left(R_{Ro}^2 + R_{mi}^2 + \frac{R_{Ro}^2 R_{mi}^2}{r^2} - \frac{(1+3\nu)}{(3+\nu)}r^2\right) \quad (6)$$

The total radial and hoop stresses in the magnet are represented as

$$\sigma_{rT_M}(r) = \frac{-P_{cont} R_{mo}^2}{(R_{mo}^2 - R_{mi}^2)}\left(1 - \frac{R_{mi}^2}{r^2}\right) + \frac{(3+\nu)}{8}\rho_m \omega_m^2 \left(R_{Ro}^2 + R_{mi}^2 - \frac{R_{Ro}^2 R_{mi}^2}{r^2} - r^2\right) \quad (7)$$

$$\sigma_{\theta T_M}(r) = \frac{-P_{cont} R_{mo}^2}{(R_{mo}^2 - R_{mi}^2)}\left(1 + \frac{R_{mi}^2}{r^2}\right) + \frac{(3+\nu)}{8}\rho_m \omega_m^2 \left(R_{Ro}^2 + R_{mi}^2 + \frac{R_{Ro}^2 R_{mi}^2}{r^2} - \frac{(1+3\nu)}{(3+\nu)}r^2\right) \quad (8)$$

where it is assumed that both inner and outer discs have the same density, modulus of elasticity and Poisson's ratio, which is entirely justified for the proposed design.

The total radial and hoop stresses in the magnet rotor disc based on the data in Table I, are obtained from equations (5-8). In addition, axisymmetric finite element (FE) stress analysis modeling of the similar structure, as shown in Fig. 4, is established to evaluate the stresses. The detailed results concerning radial and hoop stress distribution obtained from
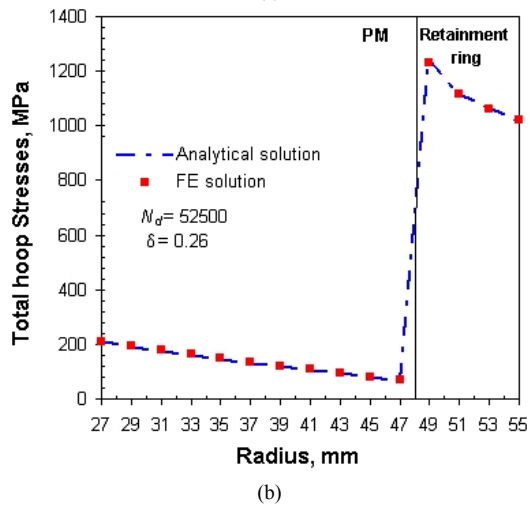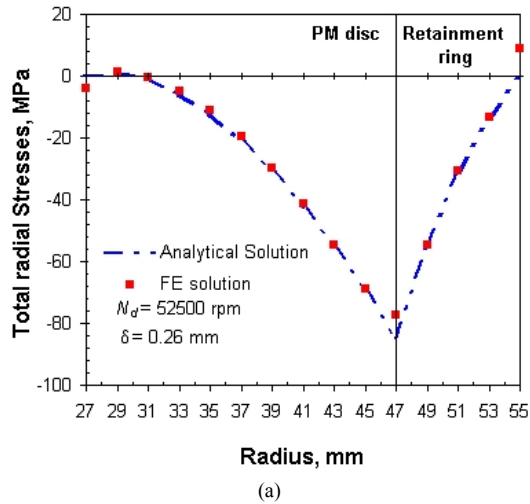
(a)

(b)

Fig. 5. Stress distribution in magnet rotor disc from the analytical and FE models, (a) total radial stress distribution, (b) total hoop stress distribution.

both models are presented graphically in Fig. 5. As can be seen from the results, good agreements between the analytical and FE models are achieved. The maximum hoop stresses at the inner radius of the retainment ring at the specified design speed (1250MPa) is below the safe design strength of the material. The hoop stresses at the inner radius of the magnet examined at design speed are found to be in excess of 209MPa, showing the risk of the magnet being damaged. However, since segmented magnets instead of continuous annular magnets are used in practice, the actual hoop stresses would be less and are estimated to be in safe limits. Moreover, the negative radial stresses at the contact surface between the magnet and retainment ring indicate that a continuous contact has been maintained at the design speed. Hence, it can be inferred that the design data in Table I could meet the design criteria and ensure mechanical integrity of the magnet rotor disc.

Due to the simplified assumptions imposed, analytical solutions are not usually suitable for complex structures. It is, however, instructive to use the analytical model to determine a feasible range for the design parameters, and then to use FE models to verify the analytical results, and to be followed by final design optimization where necessary. The rotor under
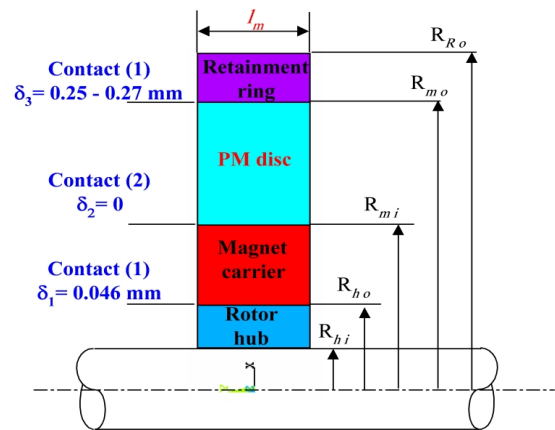
Fig. 6. Simplified magnet rotor disc for the 2-D parametric axisymmetric FE stress analysis.

TABLE II
DESIGN DATA FOR PARAMETRIC 2-D FE STRESS ANALYSIS

R_{hi} mm	R_{ho} mm	R_{mi} mm	R_{mo} mm	R_{Ro} mm	l_m mm	δ_l mm	δ_2 mm	δ_3 mm
7.5	14	27	47	49-65	17	0.046	-	0.25-0.27

study is a complex structure comprising segmented magnets with specific geometries. For complex structures, 3-D FE models are required to evaluate the stresses accurately. However, 3-D FEA will take extensive computational time and therefore not practical for parametric study. Consequently 2-D parametric analysis is performed for a simplified rotor model with four concentric discs as shown in Fig. 6. The purpose of the parametric analysis is to investigate the influence of varying the retainment ring radial thickness on the mechanical integrity of the magnet rotor disc. The design data and mechanical properties for the materials in the analysis are given in Table II and Table VI in Appendix respectively. The outer radius of the retainment ring is varied over the range of 49-65mm with an increment step of 2mm while the interference fit between the retainment ring and magnet is also varied in the range from 0.250-0.270mm with an increment step of 0.010mm.

For contact status, the radial stresses are checked at the place of contact between the magnet and magnet carrier. Preliminary results by analytical solutions show that the chance of detachment at that place are much higher than in any other places, as be deduced from the values of radial stress results at R_{mi} as seen in Fig.7(a), and from the maximum hoop stresses at the inner surface of the retainment ring, R_{mo}, as seen in Fig.7(b). It can be observed from the results that for a particular magnet rotor disc, there is an optimum thickness for the retainment ring where hoop and radial stresses can be suppressed to their minimum values. The stresses are decreased as the retainment ring radial thickness is increased, starting from 2mm up to a certain thickness where the stresses start to increase again, which is expected since the centrifugal forces due to the increased mass of the ring will be raised as the ring thickness increases. Thus, the more positive pressure at the retainment ring inner surface is developed, the more radial growth and expansion will occur. On the other hand, it can also be seen that increasing the interference fit is beneficial from the design
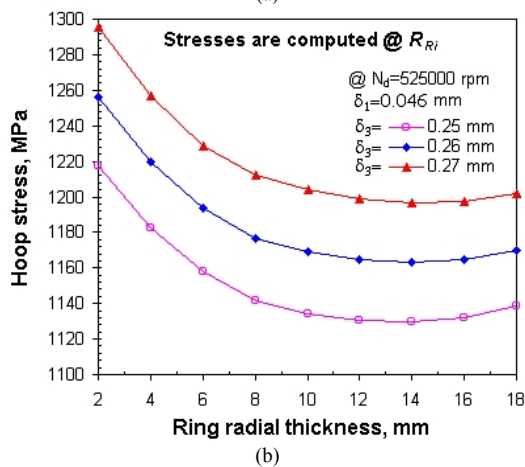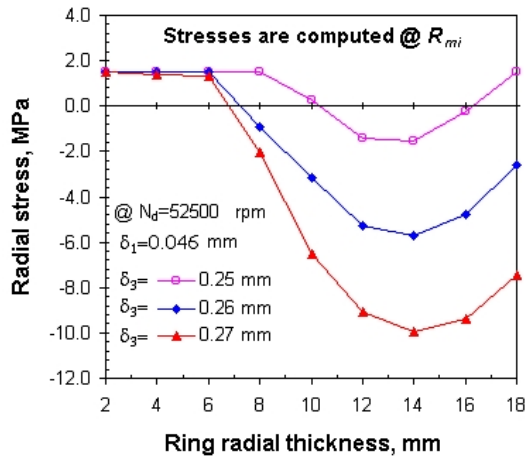
(a)

(b)

Fig.7. Stresses computed for different retainment ring thicknesses and interference fits at 52500rpm, (a) radial stresses at magnet inner radius, (b) hoop stresses at retainment ring inner radius.

(a)

(b)

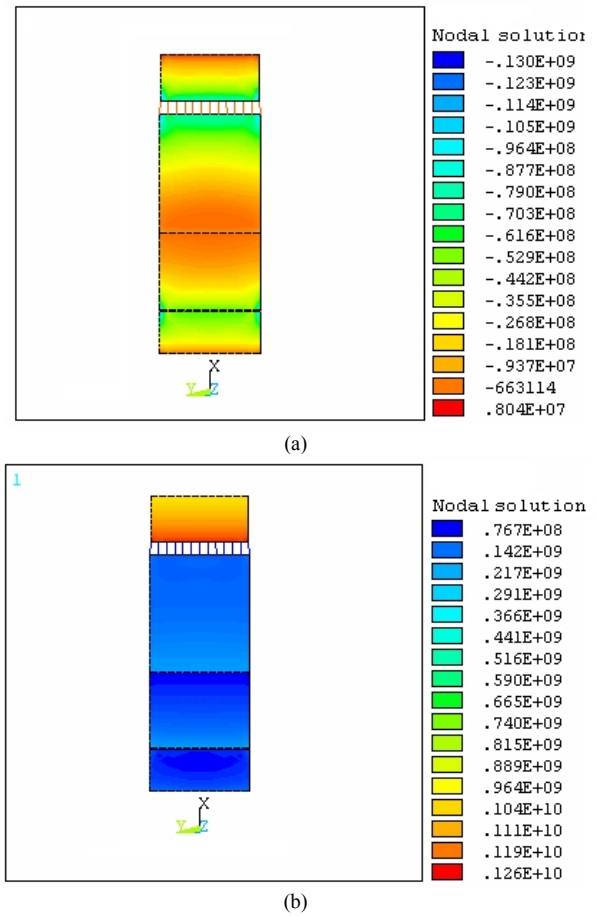Fig.8. The radial and hoop stress contours for the selected design at 52500rpm, (a) radial stress contours, (b) hoop stress contours.

point of view. With higher interference fit, retainment rings with less thickness can be used to achieve a certain compressive radial stress. Hence, a continuous contact can be achieved at the required surface.

However, precautions should be taken when choosing higher values of interference fit due to two reasons:

- any increase in the interference fit would increase the hoop stresses at inner surface of the retainment ring, which may be approaching the level of the specified design strength;
- high interference fit values would result in high temperature differences to allow for the required expansion, which may deteriorate mechanical and physical properties, and ultimately the strength of the materials.

Consequently, the interference fit of 0.260mm is selected for the current design. For the specified interference fit value, the minimum stresses can be achieved with a retainment ring radial thickness 14mm. Although mechanical integrity is the most important design criteria for such a high-speed generator, other related aspects such as ultimate compactness, lightness and high performance must also be considered in the design process. It is of particular interest to minimize the size and weight of the

retainment ring provided that mechanical integrity can be achieved when determining the retainment ring radial thickness. It can be found that for the selected value of interference fit, a radial thickness 8mm is selected for the retainment ring. This value ensures a continuous contact at the surface between the magnet and magnet carrier. The radial and hoop stress contours from 2-D FEA for the selected design are shown in Fig. 8.

Finally, 3-D FE stress validations taking into account the unsymmetrical and non-homogeneous structure have been carried out for the actual magnet rotor disc with segmented semicircular magnets [4]. In order to minimize extensive computational time, only one-eighth of the disc with symmetric boundary condition is modeled as Fig. 9, which is constrained at specified nodes to prevent rigid body motion in z-direction. The evaluated radial and hoop stress contours are illustrated in Fig. 10. It can be seen that the stresses are not uniformly distributed in the rotor especially at the inner surface of the retainment ring.

For more precise results, the radial and hoop stresses obtained from the 3-D model are computed at two different positions. The first results are obtained along the radial coordinates of the disc where only magnet carrier is in contact with the retainment ring, at position $z=0$ and $\theta=0$ degree, while the second ones are derived along the same radial coordinates but with angular coordinates shifted to the centre of the magnet,
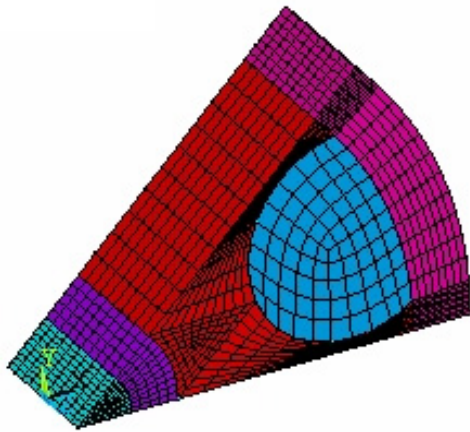
Fig. 9. Meshed 3-D FE stress model for one-eighth of the magnet rotor disc.
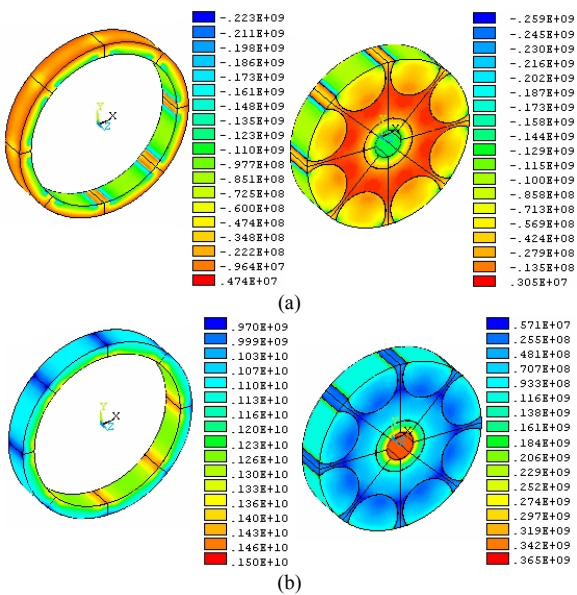

(a)

(b)

Fig. 10. The 3-D radial and hoop stress contours for the selected design at 52500rpm, (a) radial stress contours, (b) hoop stress contours.

at position z=0 and θ=22.5degree where the magnet is in contact with the retainment ring. The radial and maximum hoop stresses at the proposed two different positions from the 3-D model together with the results from the previous axisymmetric 2-D model are compared in Fig. 11, which shows that there are some discrepancies between the results from the two models and the discrepancies vary according to the place even in the same 3-D model. These can be explained by the fact that there are two different materials in contact with the ring at different angular positions. Thus, a non-homogenous pressure is exerted on the inner surface of the retainment ring and as a result non-uniform stress distribution is generated. Higher hoop and radial stresses are found at the position θ=0degree, which can be referred to the increased radial growth at the magnet carrier rim due to the lowest Young's modulus. The maximum hoop stress at position θ=0degree is 5% more than that obtained at position θ=22.5 degree. Also the maximum hoop stress from the axisymmetric 2-D FE model is 7% and 2% less than those gained at the first and second positions respectively from the 3-D FE model. Most importantly, the maximum hoop stress is

(a)

(b)
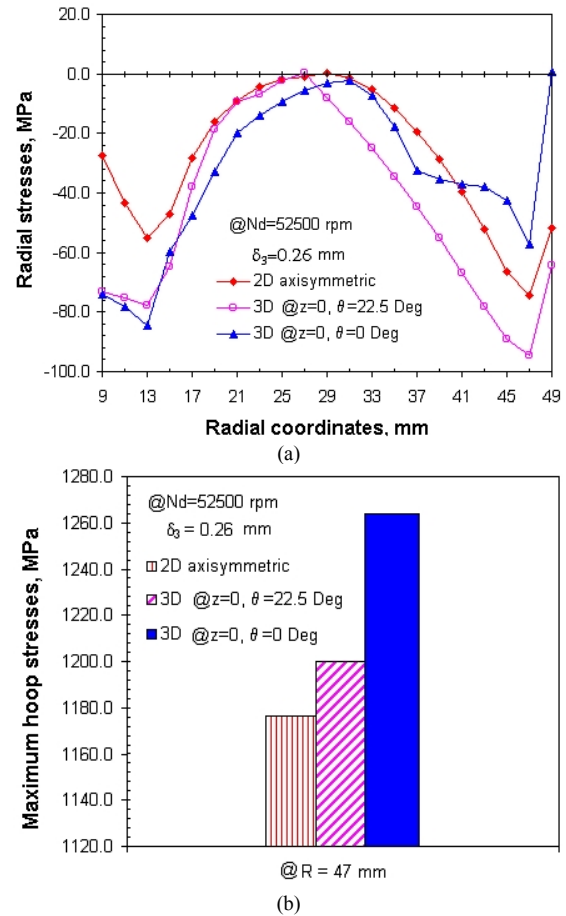
Fig. 11. Comparisons of the radial and maximum hoop stresses between the 2-D axisymmetric and 3-D models, (a) radial stresses, (b) maximum hoop stresses.

within the safe design strength of the specified material and negative radial stresses are maintained at all the contact surfaces, confirming continuous contacts. However, there are discrepancies in the negative radial stresses due the non-homogenous geometry.

It can be concluded that the 2-D axisymmetric FE model is reliable and the computed results can be accepted and used with reasonable confidence for first order evaluation of the mechanical integrity during the early stage of the design process. However, 3-D FE models will be necessary for mechanical integrity assessment at the advanced design stage.

IV. BACK IRON DISC DESIGN

The back iron, normally called the keeper disc, is the part which completes the magnetic circuit in electric machine. As such, it is an integral part of the rotor unit. In general, laminations are employed for the back iron to minimize the eddy current losses. However, in high-speed applications, laminated sheets are not suitable for the rotor structure since they can be a source of mechanical failure due to the high centrifugal forces exerted on those parts. In addition, epoxy resin and sometimes tie rods and bolts are required for the stacking process and mechanical support of the laminated structure, which could complicate the design.
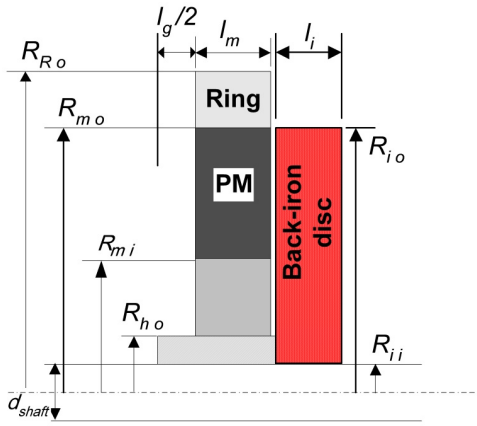
Fig. 12. Simplified view of the magnet rotor disc assembly and back iron disc.
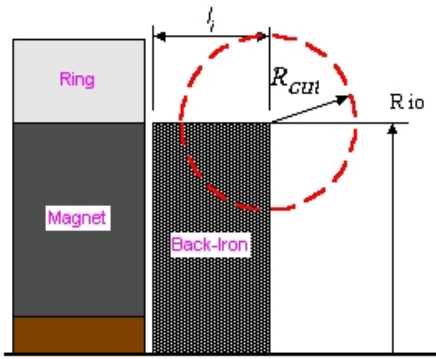

Fig. 13. Profiling of the back iron disc, circular cutting.

Fig. 14. 2-D axisymmetric FE model for the profiled back iron disc.

$$\sigma_{r1} = -P_{cont} \tag{11}$$

$$\sigma_{\theta1} = P_{cont} \frac{R_{io}^2 + R_{ii}^2}{R_{io}^2 - R_{ii}^2} \tag{12}$$

It is noted that the disc-shaft assembly acts as a single solid disc until the shrink fit loosens. Thus, the associated stresses for a solid rotating disc can be derived as

$$\sigma_{r2} = \frac{3+\nu}{8} \rho \omega^2 R_{io}^2 \left(1 - \frac{r^2}{R_{io}^2} \right) \tag{13}$$

$$\sigma_{\theta2} = \frac{3+\nu}{8} \rho \omega^2 R_{io}^2 \left(1 - \frac{1+3\nu}{3+\nu} \frac{r^2}{R_{io}^2} \right) \tag{14}$$

Finally, the net stresses are calculated by combining both cylinder and solid disc solutions. The compressive contact pressure on the disc bore decrease as the rotational speed increases. The net radial stress at $r=R_{ii}$ becomes zero when the shrink fit loosens, so the required contact pressure to keep the disc rotating with the shaft can be computed as

$$P_{cont} = \frac{3+\nu}{8} \rho \omega^2 R_{io}^2 \left(1 - \frac{R_{ii}^2}{R_{io}^2} \right) \tag{15}$$

Consequently, the net tangential stress at $r=R_{ii}$ can be derived as

$$\sigma_{\theta T} = \frac{3+\nu}{8} \rho \omega^2 \left[(R_{io}^2 + R_{ii}^2) + R_{io}^2 \left(1 - \frac{1+3\nu}{3+\nu} \frac{R_{ii}^2}{R_{io}^2} \right) \right] \tag{16}$$

The minimum amount of the shrink fit required to keep the disc in contact with the shaft can be found as

$$\delta = \frac{P_{cont} \sqrt{R_{io}^2 R_{ii}^2}}{E} \tag{17}$$

Silicon iron is selected for the back iron disc due to its relatively low cost, good magnetic and mechanical properties, which are given in Table VII in Appendix. Based on the electromagnetic analysis and equations (9-17), the design data for the uniform back iron disc is given in Table III.

In this paper, a solid disc form of the back iron is proposed for the high-speed application, not only because of its rigidity, mechanical integrity and robustness, but also because of simplicity and cost reduction in manufacture and assembly. Moreover, since the magnet rotor is rigidly fixed with the back iron, the eddy current losses due to space harmonics are minimized. The back iron usually takes the form of uniform circular disc shown in Fig.12. In order to further reduce the weight and hence mechanical stress at high speed, a profiled circular disc shown in Fig.13 will be investigated.

However, the design data for the uniform disc must be first developed. The back iron disc is fitted on the shaft via shrink fit to prevent slippage at high-speed operation. In Fig.12, when the disc is standstill, a contact pressure P_{cont} is exerted on the disc bore. The residual radial and tangential stresses can be calculated using Lame solution for thick-walled cylinder theory [25] as

$$\sigma_{r1} = \frac{P_{cont} R_{ii}^2}{R_{io}^2 - R_{ii}^2} \left(1 - \frac{R_{io}^2}{r^2} \right) \tag{9}$$

$$\sigma_{\theta1} = \frac{P_{cont} R_{ii}^2}{R_{io}^2 - R_{ii}^2} \left(1 + \frac{R_{io}^2}{r^2} \right) \tag{10}$$

where R_{io} and R_{ii} are the outer and inner radii of the back iron disc respectively, and r is the radius where stress is calculated. The maximum radial and tangential stresses occur at the bore of the disc ($r=R_{ii}$) as
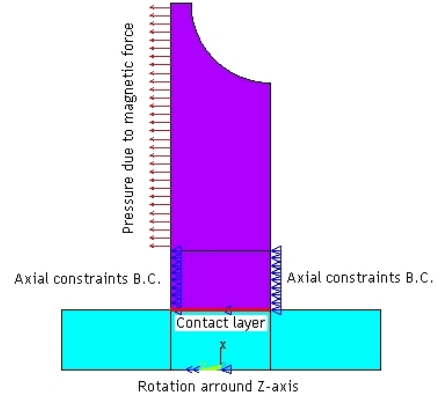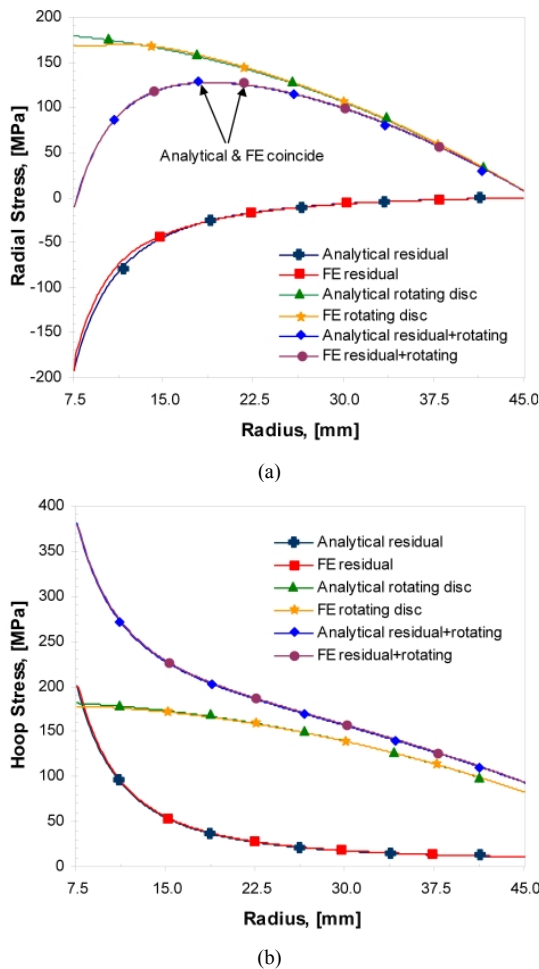
(a)

Fig. 15. Comparisons of the radial and hoop stresses for the uniform back iron disc between the analytical and 2-D axisymmetric models, (a) radial stresses, (b) hoop stresses.
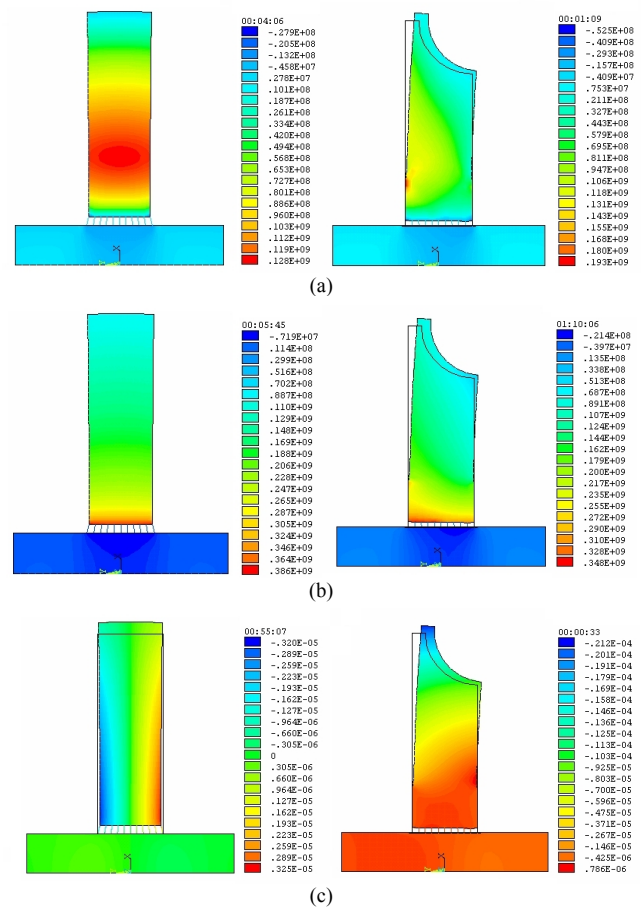
(b)

(a)

(b)

(c)

Fig. 16. Radial and hoop stress contours and lateral deflection comparisons between the uniform and profiled back iron discs, (a) radial stress contours, (b) hoop stress contours, (c) lateral deflection.

TABLE III
DESIGN DATA FOR UNIFORM BACK IRON

R_{io} mm	R_{ii} mm	l_i mm	P_{cont} MPa	δ μm	$\sigma_{\theta 1}$ MPa	$\sigma_{\theta 2}$ MPa	$\sigma_{\theta 3}$ MPa
46	7.5	12.5	188.5	16.8	198.4	190.6	390

The profiled configuration is by means of circular cut-away of the uniform disc as illustrated in Fig.13. The optimal R_{cut} can be derived as 10mm from the electromagnetic FE analysis. A clearance gap 0.5mm is set between the back iron disc and magnet rotor disc for mechanical isolation when they are running at high rotational speed. The attraction force per unit depth can be predicted by the 2-D FE model as 13551N/m.

The FE model for the profiled disc with all boundary conditions and possible loads applied is shown in Fig. 14. For the purpose of comparison, the FE stress analysis is performed on both the simple back iron disc of uniform thickness and the profiled disc with a 10mm circular cutting. The radial and hoop stress results of the uniform disc from analytical equations and FE model are compared in Fig. 15, which shows good agreements. The contour plots for the radial and hoop stresses and lateral deflections for both types of the back iron disc are compared in Fig. 16. From the plots, it can be seen that the maximum hoop stresses at the bore of the uniform and profiled

discs are 386MPa and 348MPa respectively. Thus, the hoop stress for the profiled disc is reduced by 9.8% for the same operating speed and shrink fit. In addition, a maximum radial compressive stresses of -8MPa is found at the bore of the profiled disc compared to -4MPa that of the uniform disc. This increase in the compressive radial stress (86%) is beneficial for the design of the back iron disc since higher compressive radial stresses implies an improvement in the binding ability of the disc on the shaft at the design speed. Accordingly, the amount of shrink fit can be further reduced, thus lower hoop stresses can be maintained as a result of profiling the back iron disc. It can also be seen that the lateral deflection at the rim of the uniform disc is almost negligible whereas a maximum negative deflection of 21.3μm is observed for profiled disc on the side next to the magnet rotor disc. This deflection provides sufficient safety margin and clearance allowance for mating parts in the final assembly.

In order to investigate the effect of shrink fit on the stresses and deflection levels at the bore of the back iron disc, both the uniform and profiled discs are examined in the range of 10-20 μm of shrink fits. At the same time, the effect of several different boundary conditions applied to the bore of the profiled disc is investigated as well. The first of those conditions is that of free disc when the profiled disc is alone
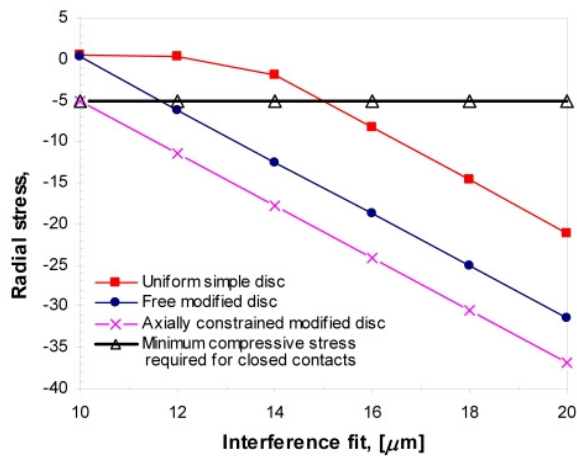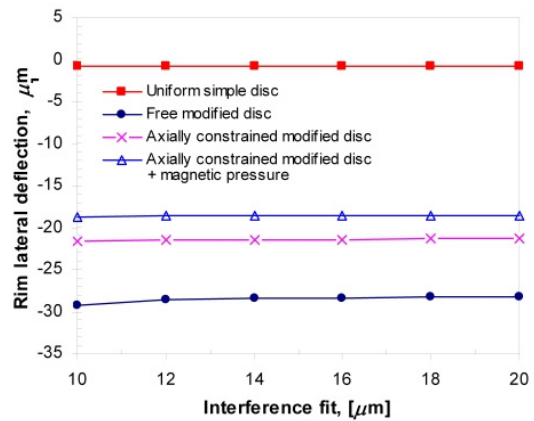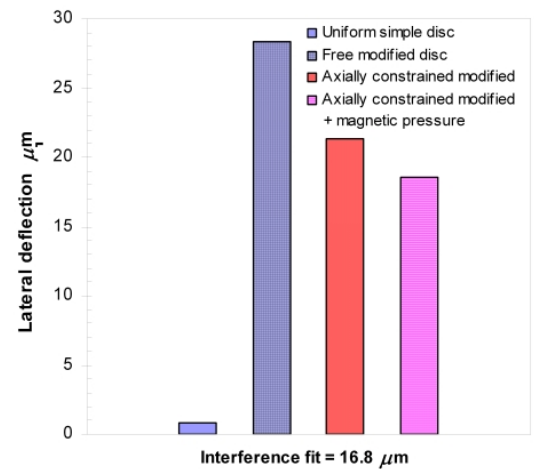
(a)
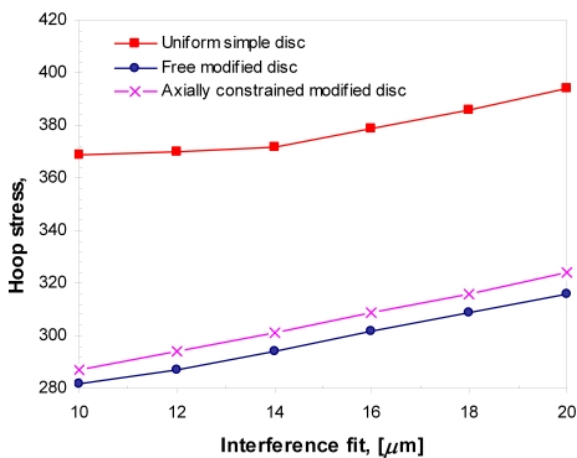
(b)

Fig. 17. Radial and hoop stresses versus shrink fit for uniform disc and profiled disc with different boundary conditions, (a) radial stresses, (b) hoop stresses.

(a)

(b)

Fig. 18. Lateral deflection, (a) lateral deflections versus shrink fit for the uniform disc and profiled disc at different boundary conditions, (b) comparison of lateral deflections for uniform and profiled disc with different boundary conditions at 16.8μm shrink fit.

shrunk onto the shaft. Hence there are no axially constraints on both sides of the disc. The second condition is that of the axial constraint disc when the disc is placed between the magnet rotor disc and the shaft nut and by tightening the nut an axial force is applied to both sides of the disc. The third involves magnetic pressure applied to the axially constraint disc. The pressure is applied to the disc surface area that is on the side opposite to the magnet rotor disc shown in Fig. 14. The radial and hoop stresses for the uniform disc and profiled disc with the first two boundary conditions versus different shrink fits are shown in Fig. 17, while lateral deflections versus different shrink fits and comparison of lateral deflections at 16.8μm shrink fit for uniform disc and profiled back iron disc with all three boundary conditions are shown in Fig. 18. As expected, more contact pressure between the back iron disk and the shaft can be achieved by increasing the amount of shrink fit since the compressive radial stress at bore of the disc is increased. A compressive radial stress of approximately 5MPa is required to ensure all the contacts elements on the bore surface of the back iron disc are closed, which implies minimum 12μm and 10μm shrink fit for free and axially constraint profiled discs respectively, and 25% and 37.5% reductions compared to the

uniform disc. Meantime, the maximum hoop stresses for the free and axially constraint profiled discs are 18.4% and 20.3% lower than that for the uniform one. Additionally, Fig. 18 shows the effect of change in shrink fit on the lateral deflections is minimal and the uniform disc possesses the minimum deflection 0.825μm, whereas the free profiled disc has the maximum of 28.31μm compared to the axially constraint one of 21.36μm for an 16μm shrink fit. However, the lateral deflection is slightly decreased to 18.54μm when magnetic pressure is added to the axially constraint profiled disc. Consequently, it is considered that these are safe values since a clearance gap 0.5mm is reserved between the back iron disc and the magnet rotor disc and enough clearance is also kept for the other mating parts such as stator casing and bearing housing.

V. MECHANICAL INTEGRITY TEST

For experimental validation of the rotor integrity design by the analytical and FE models, a relatively simple cold test rig is setup as shown in Fig. 19. It comprises a small radial turbine driving the magnet rotor disc with the retainment ring. The omission of the back iron would simplify the validation
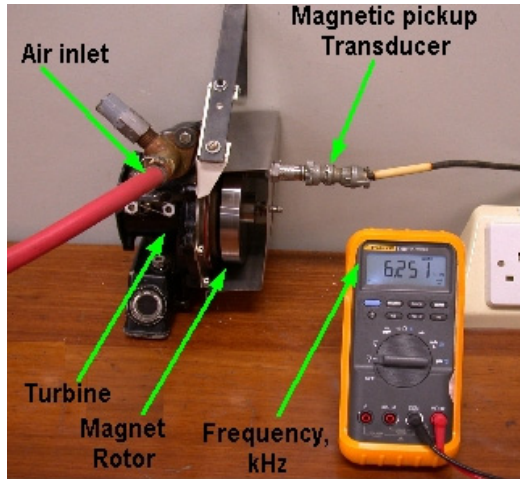
Fig. 19. Part of the cold test rig used for testing the magnet rotor disc for its mechanical integrity at 47000rpm.

significantly without loss of generality. Moreover, the magnet rotor with the retainment is a far more complex structure than the back iron, and therefore presents as the most crucial part of validation. The magnet rotor disc is mounted, at the pre-magnetised stage, on the same shaft of the turbine rotor. Controllable pressurised air is used to propel the turbine at different speeds. A maximum speed of 47000 rpm, sufficiently close to the designed speed of 50000rpm for the purpose of validation, could be achieved by the turbine. A pre-calibrated magnetic pickup transducer is used to measure the speed of the rotor. A digital multimeter reads the maximum frequency of the output signal from the magnetic pickup to be 6.251kHz, as shown in Fig. 19, at the maximum speed. For an 8-pole machine, this corresponds to 781.4Hz or 46882 rpm. The test has been repeated several times to operate the rotor under different conditions such as varying rates of acceleration and deceleration. Also the rotor was operated at the maximum speed of 47000rpm for a prolonged time of over 2 hours. The various tests undertaken confirm the rotor is mechanically robust. During the acceleration of the rotor to the maximum speed, slight vibrations of the rotor were observed at 22,300 rpm and 39,000 rpm respectively. Apart from these two speeds, the rotor was running smoothly without experiencing any noticeable vibration.

VI. CONCLUSION

A comprehensive mechanical analysis and design of the rotor discs for a high-speed air-cored AFPM generator suitable for many mission critical applications is presented. The study provides a timely complement to similar work already established for radial flux machines in the literature. The proposed systematic and vigorous design methodology adopts a two-stage approach, using an analytical and 2D-FE modeling for preliminary design and further optimization, and then 3D FE modeling and experimental tests on a prototype for final validation of the overall design. The experimental validation will be extended to cover the overall assembled rotor with different loading conditions for the completeness of the study in the future.

TABLE IV
SPECIFICATIONS OF EN24T STEEL

Density (ρ_m)	Tensile strength (σ_U)	Young's modulus (E)	Shear modulus (G)	Poisson's ratio (ν)
7.8 g/cm^3	700 MPa	200 GPa	87 GPa	0.29

TABLE V
SPECIFICATIONS OF MARAGING G125

Density (ρ_m)	Yeild strength (σ_{Ty})	Young's modulus (E)	Elongation percentage	Poisson's ratio (ν)
7.9 g/cm^3	1950 MPa	195GPa	10%	0.3

TABLE VI
MECHANICAL PROPERTIES OF THE MATERIALS FOR FE STRESS ANALYSIS

Part	Material Type	ρ (kg/m^3)	E (GPa)	υ	μ_u
Rotor hub	17/4 PH steel	7800	210	0.3	0.4
Magnet carrier	Alumec 79	2750	71	0.29	0.4
Magnet	Sintered NdFeB	7500	160	0.3	0.4
Retainment ring	Maraging G125	7900	195	0.3	0.4

TABLE VII
SPECIFICATIONS OF SILICON IRON

Density (ρ_m) g/cm^3	Yeild strength (σ_{Ty}) MPa	Young's modulus (E) GPa	Elong-ation %	Poisson's ratio (ν)	Magnetic saturation (T)
7.85	517	210	30	0.3	2.06

REFERENCES

[1] K. R. Pullen, M. R. Etemad, and A. Fenocchi, "The high speed axial flux disc generator-unlocking the potential of the automotive gas turbine," in *Proc. IEE Colloq. Machines & Drives for Electric and Hybrid Vehicles*, 1996, pp. 8/1-8/4.

[2] J. F. Gieras, R. J. Wang, and M. J. Kamper, *Axial Flux Permanent Magnet Brushless Machines*, 2nd ed., Springer, 2008.

[3] T. S. El-Hasan, P. C. K. Luk, F. S. Bhinder, and M. S. Ebaid, "Modular design of high-speed permanent-magnet axial flux generator," *IEEE Trans. Magn.*, vol. 36, no. 5, pp. 3558-3561, Sep. 2000.

[4] T. S. El-Hasan, and P. C. K. Luk, "Magnet topology optimization to reduce harmonics in high speed axial flux generators," *IEEE Trans. Magn.*, vol. 39, no. 5, pp. 3340-3342, Sep. 2003.

[5] W. Fei, and P. C. K. Luk, "Design of a 1kW high speed axial flux permanent-magnet machine," in *Proc. IET Power Electronics, Machines & Drives Conf.*, 2008, pp. 230-234.

[6] M. Sadeghierad, A. Darabi, H. Lesani, and H. Monsef, "Rotor yoke thickness of coreless high-speed axial-flux permanent magnet generator," *IEEE Trans. Magn.*, vol. 45, no. 4, pp.2032-2037, April 2009.

[7] W. Fei, and P. C. K. Luk, "Design and performance analysis of a high-speed air-cored axial-flux permanent-magnet generator with circular magnets and coils," *Proc. IEEE int. Eletric Machines & Drives conf.*, pp.1-10, 2009.

[8] R. J. Hill-Cottingham, P. C. Coles, J. F. Eastham, F. Profumo, A. Tenconi, and G. Gianolio, "Multi-disc axial flux stratospheric aircraft propeller drive," in *Proc. IEEE Industry Applications. Conf.*, 2001, pp. 1634-1639.

[9] R. J. Hill-Cottingham, P. C. Coles, J. F. Eastham, F. Profumo, A. Tenconi, and G. Gianolio, "Novel axial flux machine for aircraft drive: design and modeling," *IEEE Trans. Magn.*, vol. 38, no. 5, pp. 3003-3005, Sep. 2002.

[10] R. J. Hill-Cottingham, P. C. Coles, J. F. Eastham, F. Profumo, A. Tenconi, and G. Gianolio, "A plastic structure multi-disc axial flux PM motor," in *Proc. IEEE Industry Applications Conf.*, 2002, pp. 1274-1280.

[11] J. R. Bumby, and R. Martin, "Axial-flux permanent-magnet air-cored generator for small-scale wind turbines," *Proc. Inst. Electr. Eng. –Electr. Power Appl.*, vol. 152, no. 5, pp. 1065-1075, Sep. 2005.

[12] T. F. Chan, and L. L. Lai, "An axial-flux permanent-magnet synchronous generator for a direct-coupled wind-turbine system," *IEEE Trans. Energy Convers.*, vol. 22, no. 1, pp. 86-94, Mar. 2007.

[13] M. J. Kamper, R. J. Wang, and F. G. Rossouw, " Analysis and performance of axial flux permanent-magnet machine with air-cored nonoverlapping concentrated stator windings," *IEEE Trans. Ind. Appl.*, vol. 44, no. 5, pp. 1495-1504, Sep./Oct. 2008.

[14] S. M. Hosseini, M. Agha-Mirsalim, and M. Mirzaei, "Design, prototyping, and analysis of a low cost axial-flux coreless permanent-magnet generator," *IEEE Trans. Magn.*, vol. 44, no. 1, pp. 75-80, Jan. 2008.

[15] S. Javadi, and M. Mirsalim, "A coreless axial-flux permanent-magnet generator for automotive applications," *IEEE Trans. Magn.*, vol. 44, no. 12, pp. 4591-4598, Dec. 2008.

[16] R. J. Wang and M. J. Kamper, "Calculation of eddy current loss in axial field permanent-magnet machine with coreless stator," *IEEE Trans. Energy Convers.*, vol. 19, no. 3, pp. 532-538, Sept. 2004.

[17] R. J. Wang, M. J. Kamper, K. V. Westhuizen, and J. F. Gieras, "Optimal design of a coreless stator axial flux permanent-magnet generator," *IEEE Trans. Magn.*, vol. 41, no. 1, pp. 55-64, Jan. 2005.

[18] L. Zheng, T. X. Wu, K. B. Sundaram, J. Vaidya, L. Zhao, D. Acharya, C. H. Ham, J. Kapat, and L. Chow, "Analysis and test of a high-speed axial flux permanent magnet synchronous motor," in *Proc. IEEE int. Electric Machines & Drives Conf.*, 2005, pp. 119-124.

[19] F. Sahin, A. M. Tuckey, A. J. A. Vandeput, "Design, development and testing of a high-speed axial-flux permanent-magnet machine," in *Proc. IEEE Industry Applications Conf.*, 2001, pp. 1640-1647.

[20] K. R. Pullen, "The design and development of a small gas turbine and high speed generator," Ph.D. dissertation, Dept. Mech. Eng., Imperial college of science, technology and medicine, University of London, 1991.

[21] T. Wang, F. Wang, H. Bai, and J. Xing, "Optimization design of rotor structure for high speed permanent magnet machines," in *Proc. Int. Conf. Electrical Machines & Systems*, 2007, pp. 1438-1442.

[22] A. Borisavljevic, H. Polinder, and B. Ferreira, "Overcoming limits of high-speed PM machines," in *Proc. Int. Conf. Electrical Machines*, 2008, pp. 1-6.

[23] E. C. Lovelace, T. M. Jahns, T. A. Keim, and J. H. Lang, "Mechanical design considerations for conventionally laminated, high-speed, interior PM synchronous machine rotors," *IEEE Trans. Ind. Appl.*, vol. 40, no. 3, pp. 806-812, May/June 2004.

[24] A. S. Hall, A. R. Holowenko, and H. G. Laughlin, *Schaum's outline of theory and problems of machine design*, SI (Metric) edition, McGraw-Hill, 1980.

[25] R. J. Roark, *Formula for stress & strain*, McGraw-Hill, 1990.